

Temperature dependence of Auger recombination in crystalline silicon from 117–463 K[☆]

Lachlan E. Black^a*, Yan Zhu^b, Ziv Hameiri^b, Daniel H. Macdonald^a

^a School of Engineering, The Australian National University, Canberra, 2600, ACT, Australia

^b School of Photovoltaic and Renewable Energy Engineering, University of New South Wales, Sydney, 2052, NSW, Australia

ARTICLE INFO

Keywords:

Crystalline silicon
Auger recombination
Solar cells

ABSTRACT

As crystalline silicon solar cells approach their theoretical limit, a better understanding of the Auger recombination processes which define this limit is required, including at temperatures away from room temperature, where most solar modules operate. In this work, we apply a recently developed approach to measure the temperature dependence of the ambipolar Auger coefficient, C_{amb} , in the range of 117–463 K at carrier concentrations relevant for solar cell operation. We observe a significant dependence of C_{amb} on temperature, decreasing with increasing temperature in the measured range. We show that disagreement between the temperature dependence observed in previous works can be explained as resulting from differences in the carrier concentration range probed by different experiments, with our results showing good agreement with previous measurements performed at lower concentrations. This can be understood in terms of the temperature and carrier concentration dependence of the Coulomb enhancement factors. We develop a semi-empirical parameterisation of Auger recombination valid for arbitrary carrier concentrations and temperatures that extends the current established room-temperature model to incorporate the observed temperature dependence. We show that consideration of the temperature dependence of Auger recombination has significant consequences for the limiting efficiency of solar cells and modules at typical operating temperatures.

1. Introduction

Auger (or Auger–Meitner [1]) recombination is the dominant intrinsic recombination process in crystalline silicon (c-Si), and limits the theoretical efficiency of c-Si solar cells [2,3]. Accurate models for Auger recombination rates in c-Si are increasingly important as c-Si cells approach this limit [4]. Recent experimental works by Black and Macdonald [2] and Niewelt et al. [3] have revised the established model for Auger recombination in c-Si near room temperature. However, these studies did not address the temperature dependence of Auger recombination. Solar modules in the field typically operate at temperatures significantly higher than standard test conditions (25 °C), with peak temperatures >70 °C for rack-mounted and >90 °C for roof-mounted systems [5]. Accurate values of the Auger coefficients in this range are therefore necessary to accurately predict real-world solar cell performance. The temperature-dependence of Auger recombination is also relevant for silicon-based power electronics devices, where components may operate at temperatures up to ~200 °C [6]. Measurements of the temperature dependence of Auger recombination at lower temperatures are also important for accurate analysis

of temperature-dependent lifetime spectroscopy measurements [7], as well as to improve understanding of the relevant physical processes.

Only a handful of previous studies have attempted to investigate the temperature dependence of the Auger coefficients in crystalline silicon [8–12]. Dziewior and Schmid [8] determined the low-injection Auger coefficients C_n and C_p in heavily doped ($\sim 10^{19} \text{ cm}^{-3}$ to 10^{20} cm^{-3}) c-Si at 77, 300 and 400 K using time-resolved photoluminescence decay measurements. They found only a rather weak dependence on temperature (increasing with absolute temperature T), with $C_n + C_p = 3.79 \times 10^{-31} \text{ cm}^6 \text{ s}^{-1}$ at 300 K. Svantesson and Nilsson [9] measured the ambipolar Auger coefficient $C_{amb} = C_n + C_p$ from 195–372 K at very high injection levels (excess carrier concentration $\Delta n \approx 2 \times 10^{18} \text{ cm}^{-3}$ to $4 \times 10^{18} \text{ cm}^{-3}$) in undoped Si by monitoring the photoluminescence decay following high-power pulsed laser excitation. They found the resulting values of C_{amb} to increase slightly with temperature with an approximate $T^{0.6}$ dependence and a value of $C_{amb} \approx 4 \times 10^{-31} \text{ cm}^6 \text{ s}^{-1}$ near room temperature, similar to the value determined by Dziewior and Schmid. Jonsson et al. [10] determined C_{amb} in the range of 300 K to 400 K from time-resolved free-carrier absorption measurements of

[☆] This article is part of a Special issue entitled: ‘SiliconPV 2025’ published in Solar Energy Materials and Solar Cells.

* Corresponding author.

E-mail address: lachlan.black@anu.edu.au (L.E. Black).

electrically injected ($\Delta n \approx 1 \times 10^{17} \text{ cm}^{-3}$ to $3 \times 10^{17} \text{ cm}^{-3}$) diode structures formed on electron-irradiated silicon (the latter to reduce the bulk SRH lifetime in order to mimic the situation in the intended power electronics application). They found C_{amb} to increase with temperature approximately according to a $T^{1.8}$ dependence, with a value of $C_{amb} \approx 1.1 \times 10^{-30} \text{ cm}^6 \text{ s}^{-1}$ at 300 K, somewhat higher than the values measured in previous work at higher concentrations. Notably, all of these studies measured C_{amb} at carrier concentrations significantly above those typically encountered in non-concentrator c-Si solar cells and all reported C_{amb} to increase with temperature.

Häcker [13] and Häcker and Hangleiter [14] reported measurements of the low-injection lifetime of n- and p-type c-Si samples with a wide range of majority carrier concentrations ($\sim 10^{15} \text{ cm}^{-3}$ to 10^{19} cm^{-3}) at temperatures between 70 and 360 K. They observed that the lifetime at lower carrier concentrations was significantly lower than would be expected based on the Auger coefficients measured at high concentrations, and that this discrepancy increased with decreasing temperature. They attributed this to spatial correlation of the electron-hole pairs (due to Coulombic attraction) into both scattering states and bound states (the latter identical with excitons), effectively increasing the Auger recombination rate at low carrier concentrations. Increasing carrier concentrations and increasing temperatures were understood to suppress this correlation via screening and thermal dissociation of correlated states respectively. Based on these measurements, Altermatt et al. [11] subsequently proposed a parameterisation of the temperature and concentration dependence of C_n and C_p . While at high carrier concentrations their model closely reproduces the values of Dziewior and Schmid and predicts a similarly weakly increasing dependence on temperature, at low concentrations it predicts significantly larger values for C_n and C_p in line with the lifetimes measured by Häcker and Hangleiter, with $C_{amb} = C_n + C_p$ decreasing strongly with temperature, approximately according to $T^{-1.5}$. Unfortunately, while this model was able to satisfactorily describe the experimental results of Häcker and Hangleiter, subsequent work has shown that the latter's lifetime values at lower carrier concentrations remained significantly limited by extrinsic recombination [2,3,15–17]. This also casts doubt on the temperature dependence described by the model of Altermatt et al. which was based on these measurements. Most recently, Wang and Macdonald [12] determined the temperature dependence of C_{amb} from 243 K to 473 K from the photoconductance lifetime measured at $\Delta n = 5 \times 10^{16} \text{ cm}^{-3}$ in a well-passivated, high-resistivity float-zone c-Si sample. Total recombination was assumed to be dominated by Auger recombination at this carrier concentration. They reported a significant decrease in C_{amb} with increasing temperature between 243 and 303 K, with an approximately constant value at higher temperatures.

The relatively small number of previous experimental investigations of the temperature dependence of C_{amb} may be explained by the fact that assessments of the Auger coefficients even at a single temperature are complicated. A particular problem is distinguishing Auger recombination from other non-radiative recombination processes, especially surface recombination. To get around this difficulty, most previous measurements of the temperature dependence of Auger recombination in c-Si have been performed in highly injected or heavily doped samples (carrier concentrations $> 10^{17} \text{ cm}^{-3}$), where Auger recombination is dominant, and surface contributions can be neglected. However, as noted above, it is well-established that the Auger coefficients at such high carrier concentrations are significantly lower than those at low concentrations due to Coulomb enhancement (spatial correlation) effects obtaining in the latter case, which are screened by free carriers at high concentrations [14]. As c-Si solar cells typically operate at much lower injection levels ($\sim 10^{15} \text{ cm}^{-3}$ to 10^{16} cm^{-3}), it is important to understand the temperature dependence of the Auger coefficients in this injection range. Meanwhile, theoretical studies are challenging due to the sensitive band-structure dependence of the Auger coefficients and the intractability of the three-particle correlation function describing the Coulomb enhancement [14].

We have recently demonstrated a novel technique for determining the ambipolar Auger coefficient with high accuracy at moderate injection levels, from measurements of a single sample with low but non-negligible surface recombination [2], by exploiting the known injection dependence of recombination at semiconductor surfaces passivated by highly charged dielectrics [18]. We previously applied this technique to measure the Auger coefficients of c-Si near room temperature, obtaining values in excellent agreement with the subsequent study of Niewelt et al. [3], which was based on a large, state-of-the-art sample set and employed a more conventional, but laborious, wafer thickness variation approach to account for surface recombination [3]. This technique lends itself to studying the temperature dependence of the ambipolar Auger coefficient in the injection range relevant for PV devices, since it avoids the need for measurements of multiple samples at each temperature to account for surface recombination.

In this work, we apply this technique to measure the ambipolar Auger coefficient as a function of temperature in the range of 117 K to 463 K, for peak excess carrier concentrations ranging from $1.8 \times 10^{15} \text{ cm}^{-3}$ to $1.5 \times 10^{16} \text{ cm}^{-3}$, depending on sample temperature. At these relatively low carrier concentrations, we observe a temperature dependence significantly different from that reported by previous studies that were performed at very high carrier concentrations, but in good agreement with the limited previous work performed at lower concentrations. We discuss the physical significance of our results and the practical consequences for solar cell performance, and provide empirical and semi-empirical (i.e. physically motivated) parameterisations for simulation and modelling applications.

2. Experimental details

Experiments were performed using one of the same lifetime samples (Sample #1) used in our previous work on Auger recombination at room temperature [2]. This sample was fabricated on a 4 inch diameter, chemically polished, $\sim 50 \Omega \text{ cm}$ n-type (100) float-zone Si wafer with a thickness of 317 μm after passivation. The wafer received a Tabula Rasa annealing treatment at 1000 °C in dry oxygen to annihilate possible nitrogen vacancies [19,20], followed by a hydrofluoric (HF) acid etch to strip the resulting silicon oxide, and standard Radio Corporation of America (RCA) clean with final HF dip prior to passivation. Surface passivation was provided by a $\text{PO}_x/\text{Al}_2\text{O}_3$ passivation stack (4.5 nm/11 nm thick) deposited in an Oxford Instruments FlexAL atomic layer deposition (ALD) reactor at 100 °C from trimethylphosphate, trimethylaluminium (TMA) and O_2 plasma [21–23]. A post-deposition anneal at 400 °C in N_2 for 10 min was used to activate the passivation. In order to fit within the temperature-controlled cryostat of the measurement system, the sample was mechanically cleaved following passivation to produce a piece $\sim 4 \text{ cm}$ wide. This will result in some additional edge recombination, however our analysis (Appendix C) indicates that the effect of this on the accuracy of the analysis is small or negligible.

Photoconductance lifetime measurements were performed using a customised lifetime tester system equipped with a temperature-controlled sample stage, which has been described in detail in previous publications [24]. The system was based on a modified Sinton Instruments WCT-120 lifetime tester. The sample stage and photoconductance coil were enclosed by a cryostat (INSTECH) with a 2.5 cm diameter quartz glass window. Heating was provided by resistive heaters within the sample stage, while cooling was provided by liquid nitrogen pumped through channels within the stage. A thermocouple within the sample stage was used as input to a temperature control loop which drove the heater output. Illumination was provided by a Xenon flash lamp incorporating a long-pass filter in order to obtain more uniform excitation through the depth of the sample.

Measurements were performed at set-point temperatures ranging from 110 K to 473 K, in steps of approximately 20 K. The choice of the lower limit was based on the lowest temperature at which sufficiently stable temperature control was found to be achievable during the

experiments. Following each temperature change, a delay of at least 30 min was allowed prior to the measurements to allow the sample temperature to reach equilibrium with the stage. The stage temperature was monitored as a function of time to confirm stabilisation following each set-point change. The actual sample temperature corresponding to a given set-point temperature was calculated using a functional relationship determined based on separate thermocouple measurements of a dedicated silicon wafer calibration sample. Full details of the temperature calibration procedure are given in [Appendix A](#). The resulting calculated sample temperature was used in all subsequent analysis.

The measured coil voltage was converted to apparent sample conductance G_{app} according to [\(A.1\)](#). The temperature-dependent calibration coefficients were determined using a set of silicon wafers with varying dark conductivity, taking into account the dependence of the coil sensitivity on sample thickness [\[25\]](#). Full details of the calibration procedure are given in [Appendix A](#). The apparent sample conductance was then converted to actual sample conductance G according to [\[25\]](#)

$$G = G_{app}(1 + W\lambda^{-1}) \quad (1)$$

where W is the sample thickness and λ is the characteristic attenuation length of the coil, which was determined as described in [\[25\]](#). The average value of Δn was then determined through an iterative solution of [\[2\]](#)

$$\Delta n = \frac{GW^{-1}q^{-1} - (\mu_n - \mu_{n,0})n_0}{\mu_n + \mu_p} \quad (2)$$

where q is the electron charge, μ_n and μ_p are the temperature- and injection-dependent electron and hole mobilities [\[26,27\]](#), respectively, and $\mu_{n,0}$ and n_0 are the electron mobility and electron concentration in equilibrium (all at the sample temperature).

The injection-dependent effective charge carrier lifetime $\tau_{eff}(\Delta n)$ was determined in the transient regime according to

$$\tau_{eff}(\Delta n) = \Delta n \left(\frac{d\Delta n}{dt} \right)^{-1} \quad (3)$$

The time derivative $d\Delta n/dt$ was determined via numerical differentiation of $\Delta n(t)$ using fourth-order Savitzky–Golay filtering with an adaptive window size. A purpose-built adaptive algorithm was used to select an appropriate window size at each point in order to avoid distortion of the decay curve at short decay times while minimising noise at longer decay times.

3. Results and analysis

[Fig. 1](#) shows the resulting $\tau_{eff}(\Delta n)$ curves as a function of sample temperature. There is a clear trend of increasing lifetime with increasing sample temperature.

As described in our previous work [\[2\]](#), the ambipolar Auger coefficient C_{amb} can be expressed as (for an n-type sample)

$$C_{amb} = \frac{d}{d\Delta n} \left[(\tau_{eff}^{-1} - \tau_{SRH}^{-1})(n_0 + \Delta n)^{-1} - C_n n_0 - B \frac{n_{i,0}^2}{n_i^2} \right] \quad (4)$$

where τ_{SRH} is the bulk Shockley–Read–Hall lifetime, and B is an injection-independent term which includes the contributions from radiative and surface recombination:

$$B = (1 - f_{reabs})B_{rad,0} + \frac{2}{W} \frac{J_{0s}}{qn_{i,0}^2} \quad (5)$$

where $B_{rad,0}$ is the radiative recombination coefficient in equilibrium, f_{reabs} is the fraction of reabsorbed radiative recombination, J_{0s} is the surface recombination current prefactor, n_i is the (injection dependent) intrinsic carrier concentration [\[28,29\]](#), and $n_{i,0}$ is the value of n_i in equilibrium, where all of these are a function of temperature. Note that in our technique B is simply treated as a fitting parameter and we do not attempt to calculate it directly or to disentangle surface and radiative components via [\(5\)](#).

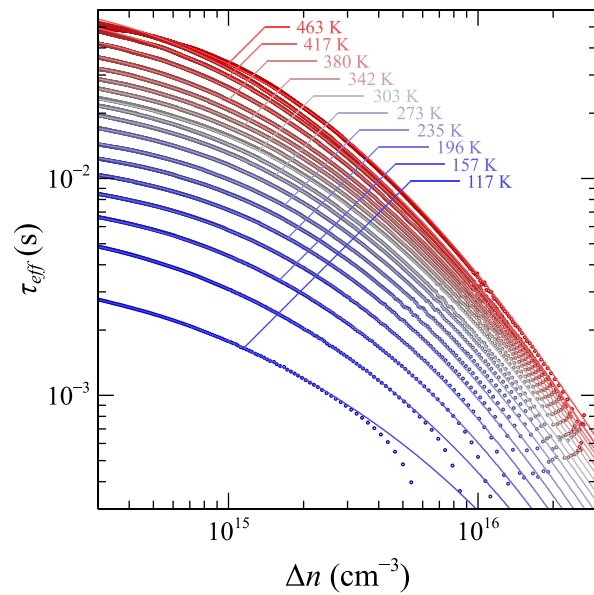


Fig. 1. Variation of measured effective lifetime τ_{eff} vs excess carrier concentration Δn with temperature ranging from 117 K to 463 K. Lines show the fits used to extract the ambipolar Auger coefficient C_{amb} .

As in our previous work [\[2\]](#), C_{amb} was determined through a two-step iterative procedure in which τ_{SRH} and B were first determined from fits of $\tau_{eff}^{-1}(n_0 + \Delta n)^{-1}$ at lower carrier concentrations with fixed C_{amb} , followed by extraction of C_{amb} from the slope of the resulting corrected inverse lifetime vs Δn at higher carrier concentrations, as described by [\(4\)](#). This procedure was iterated to achieve self-consistency of C_{amb} . For the examined sample, $C_{n}n_0$ was sufficiently low to be assumed negligible (with any slight contribution essentially absorbed in B), which avoids the need to make assumptions about the relative contributions of C_n and C_p . Extraction of C_{amb} was performed at higher carrier concentrations to limit the influence of any error in τ_{SRH} and B , while restricting the upper end of the fitted range to avoid obvious regions of non-linearity at the highest concentrations, where the uncertainties in the mobility model are also larger. As a result, the upper limit used for the fit of [\(4\)](#) varied with temperature, increasing from $1.8 \times 10^{15} \text{ cm}^{-3}$ at 117.8 K to $1.5 \times 10^{16} \text{ cm}^{-3}$ at 463.3 K. The resulting fit at each temperature together with the fitting range used are shown in [Fig. B.11](#).

[Fig. 2](#) shows the resulting extracted values of C_{amb} as a function of sample temperature. The data follow a clear trend with relatively little scatter. C_{amb} is found to decrease strongly with increasing temperature up to 300 K, and decrease somewhat less strongly with increasing temperature in the range of 300 K to 400 K, before appearing to roughly level out above 400 K. Over the examined temperature range, the extracted C_{amb} varies by exactly an order of magnitude, from $1.33 \times 10^{-29} \text{ cm}^6 \text{ s}^{-1}$ at 117 K to $1.33 \times 10^{-30} \text{ cm}^6 \text{ s}^{-1}$ at 463 K. The observed $C_{amb}(T)$ dependence is well-described by the following empirical expression:

$$C_{amb} = 2.290 \times 10^{-31} \left\{ 1 + 811.7 \exp \left[- \left(\frac{T}{18.17} \right)^{0.6498} \right] \right\} \left(1 + \frac{T}{122.6} \right) \quad (6)$$

where T is in units of Kelvin. This expression describes the measured $C_{amb}(T)$ values with a relative error less than 2.2% over the entire examined temperature range, and smaller than 1.3% for temperatures below 420 K. Eq. [\(6\)](#) results in values of $2.11 \times 10^{-30} \text{ cm}^6 \text{ s}^{-1}$ at 300 K and $2.07 \times 10^{-30} \text{ cm}^6 \text{ s}^{-1}$ at 303.15 K (30 °C), in excellent agreement with the values of $2.11 \times 10^{-30} \text{ cm}^6 \text{ s}^{-1}$ reported in our previous work [\[2\]](#) and the value of $2.06 \times 10^{-30} \text{ cm}^6 \text{ s}^{-1}$ reported by Niewelt et al. [\[3\]](#), which were both measured in the vicinity of 300 K, but without precise temperature control.

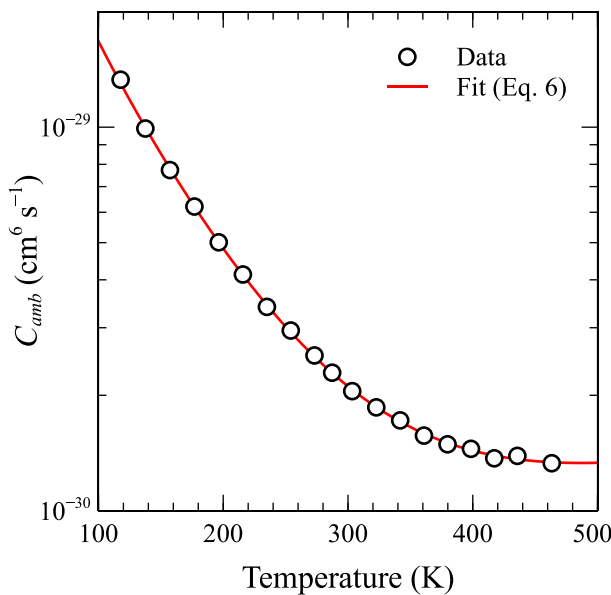


Fig. 2. Extracted C_{amb} as a function of sample temperature. The line shows an empirical fit to the data via Eq. (6).

4. Comparison to literature data

Fig. 3 compares this observed dependence with previously reported data as well as empirical and theoretical models concerning the temperature dependence of C_{amb} . It is clear that the data and models may be grouped into two categories, depending on the carrier concentration range involved. Data measured at high carrier concentrations ($\gtrsim 10^{18} \text{ cm}^{-3}$), such as those of Dziewior and Schmid [8] and Svantesson et al. [9], show lower values of C_{amb} , weakly increasing with temperature. These data are consistent with the recent first-principles calculations of Bushick and Kioupakis [30], which were calculated under low-injection conditions at a fixed majority carrier concentration of 10^{18} cm^{-3} and importantly do not include the effects of Coulomb-enhancement. Meanwhile, data measured at concentrations $\lesssim 10^{17} \text{ cm}^{-3}$, such as our own and those of Wang and Macdonald [12], as well as the model of Altermatt et al. which was based on data measured in this range, show significantly higher values and a decreasing temperature dependence. Indeed, our own data is in good qualitative agreement with the measurements of Wang and Macdonald [12], confirming the decrease in C_{amb} with temperature observed by the latter between 243 K and 390 K. The two data sets even show excellent quantitative agreement above 390 K, with a similar saturation of C_{amb} . The observed trend of C_{amb} with temperature is also in good qualitative agreement with the model of Altermatt et al., though it should be noted that the agreement is not quantitative as the latter predicts much larger values of $C_{amb} = C_n + C_p$ (the curve shown in Fig. 3 has been scaled by a factor of 0.115 to match our data at 300 K for comparison purposes).

The difference between the values of C_{amb} observed at low and at high carrier concentrations can be attributed to Coulomb-enhancement of the Auger recombination rate (i.e. due to spatial correlation of the electron and hole populations) at low concentrations, as earlier discussed. As Fig. 3 makes clear, this implies that the Coulomb-enhancement effect is stronger at lower temperatures, which is consistent with the experimental observations and first-principles calculations of Häcker and Hangleiter [14].

The data of Jonsson et al. which were measured in the intermediate injection range between 10^{17} cm^{-3} and 10^{18} cm^{-3} , appear to show intermediate behaviour, with larger values but an increasing trend with temperature. Their values at higher temperatures are significantly

higher than those obtained by Wang and Macdonald or our own data, and their quantitative reliability is questionable, particularly given the unfortunate decision by these authors to perform these measurements in electron-irradiated samples, which directly limited sensitivity to C_{amb} by increasing extrinsic recombination. Nevertheless, the qualitative trend is consistent with the expectation that the carrier concentration threshold for the onset of significant screening of the Coulomb enhancement will increase with increasing temperature, as both theoretically predicted and experimentally observed in the two-particle case [31]. Thus, it is reasonable to expect that measurements at concentrations in the range of 10^{17} cm^{-3} may well be subject to significant screening at 300 K, reducing C_{amb} , while at higher temperatures the same carrier concentrations may result in negligible screening, with C_{amb} approaching its low concentration value.

5. Development of a comprehensive model

While Eq. (6) provides a good empirical description of our data for C_{amb} , it does not allow one to distinguish either (1) the various contributions to the temperature dependence (e.g. phonon emission and absorption vs Coulomb enhancement), or (2) the relative contributions of the electron-electron-hole (eeh) and electron-hole-hole (ehh) processes (i.e. C_n and C_p). Both of these are necessary in order to develop a general model valid across the full range of carrier concentrations and temperatures in arbitrarily doped material. Therefore, we consider it important also to develop alternative semi-empirical (i.e. physically motivated) expressions which explicitly distinguish these components in a way consistent with the available data. Specifically, in the following we make use of our results to extend the model of Niewelt et al. which is currently the most widely accepted Auger model at 300 K, to incorporate the temperature dependence of both the screened Auger coefficients and the Coulomb enhancement factors.

As a basis for the temperature dependence of the screened (i.e. high-concentration) Auger coefficients, we rely on the recent first-principles calculations of Bushick and Kioupakis [30]. These represent the first such calculations to be based on the full band structure while including both direct and phonon-assisted processes, and show excellent quantitative agreement with measured values of the Auger coefficients in both n- and p-type silicon at high dopant concentrations [8], as well as with the values of C_{amb} measured by Svantesson et al. in highly injected material [9]. Early theoretical calculations of the Auger rates in silicon found values for the direct Auger process orders of magnitude too small to explain measured values [32,33], while calculated rates for the phonon-assisted process [34,35] showed good agreement with experiment, especially in the case of the ehh process, leading to the conclusion that phonon-assisted Auger recombination must be dominant [33–36]. However, these early studies included multiple simplifying approximations that significantly affected the calculated values [30,37,38]. More recent calculations performed at a more rigorous level of theory [37–39] were restricted to the direct case due to computational limitations. On the basis of reasonable quantitative agreement obtained with experiment in the eeh case, these works concluded that this process was dominated by direct transitions, with phonon-assisted transitions inferred to be important only in the ehh case [37–39]. In contrast, a key conclusion of the more comprehensive work of Bushick and Kioupakis is that phonon assisted Auger processes account for the majority of recombination in both the eeh and ehh cases, with however a significant minority contribution (~27%) from the direct Auger process in the eeh case.

Bushick and Kioupakis have parameterised the temperature dependence of the Auger coefficients for the direct and phonon-assisted eeh and ehh processes predicted by their model at a carrier concentration of 10^{18} cm^{-3} [30]. Their parameterisation for the phonon-assisted components includes two phonon emission terms and two phonon absorption terms for each process. However, we find that the resulting sum can be well-approximated in both the eeh and ehh cases (relative error <1% for

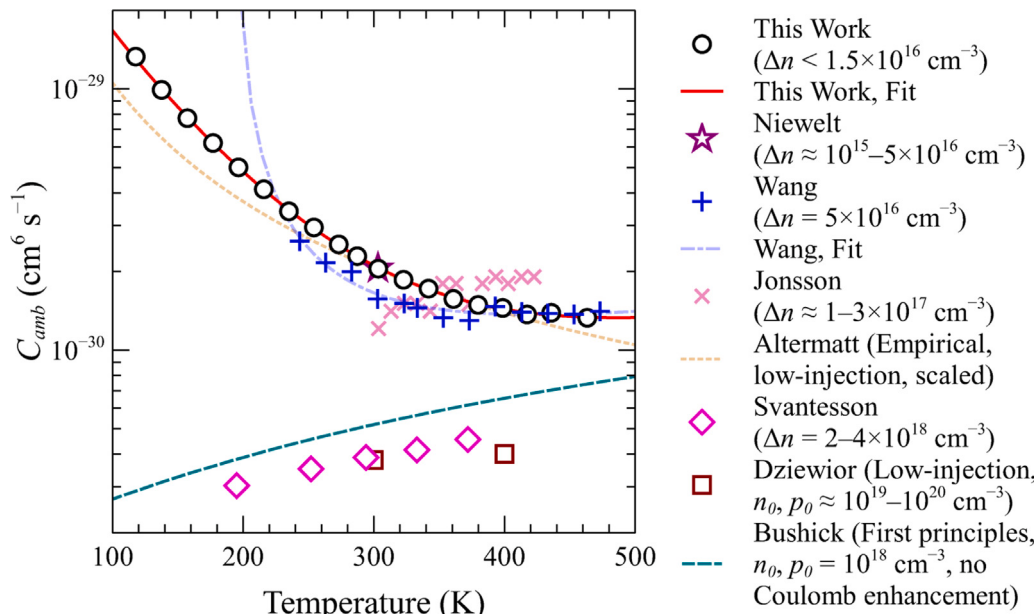


Fig. 3. Comparison of C_{amb} vs temperature determined in this work to previous experimental data (symbols) and theoretical or empirical models determined under different injection conditions and assumptions. Note that for comparison purposes the empirical model of Altermatt et al. has been scaled to match our measurements at 300 K.

$T > 80$ K) by a single combined phonon emission/absorption term with an “apparent” phonon energy, which simplifies the overall expression considerably without significant loss of accuracy. The resulting Auger coefficient for the phonon-assisted process is given by

$$C_{exh,pa} = C_{0,exh,pa} \left\{ 1 + 2 \left[\exp \left(\frac{\hbar\omega_{exh}}{kT} \right) - 1 \right]^{-1} \right\} \quad (7)$$

Here the subscript *exh* stands for either *eeh* or *ehh* depending on the relevant process, $C_{0,exh,pa}$ is the value of $C_{exh,pa}$ at 0 K and $\hbar\omega_{exh}$ is the apparent phonon energy, with $\hbar\omega_{eeh} = 21.2$ meV and $\hbar\omega_{ehh} = 21.0$ meV. Meanwhile the Auger coefficient for the direct *eeh* component is given by

$$C_{eeh,dir} = C_{0,eeh,dir} \exp \left(-\frac{E_{a,eeh}}{kT} \right) \quad (8)$$

where $E_{a,eeh} = 2.8$ meV is the activation energy given by Bushick and Kioupakis and $C_{0,eeh,dir}$ the pre-exponential factor for the direct *eeh* process. The direct *ehh* component is negligible and can be ignored. The total screened Auger coefficients are then given by the sum of the direct and phonon-assisted components:

$$C_{n0} = C_{eeh,dir} + C_{eeh,pa} \quad (9)$$

$$C_{p0} = C_{ehh,pa} \quad (10)$$

Taking this parameterisation as our starting point for the temperature dependence of the screened coefficients, we next seek to maintain consistency with the model of Nieuwelt et al. [3] at high concentrations by adjusting the relative weighting of the screened coefficients given by Bushick and Kioupakis. Specifically, we adjust $C_{0,eeh,pa}$, $C_{0,ehh,pa}$, and $C_{0,eeh,dir}$ in order to match the resulting C_{n0} and C_{p0} at 300 K with the values used in the model of Nieuwelt et al. [3], which derive from our own revision of the data of Dziewior and Schmid [2]. Here we assume that the ratio between $C_{0,eeh,dir}$ and $C_{0,eeh,pa}$ remains equal to that given by Bushick and Kioupakis, so that the relative contribution of direct and phonon-assisted components to the *eeh* process is unaffected. This results in a slight increase of $C_{n0}(T)$ by 7 %, and a more significant reduction of $C_{p0}(T)$ by 42 %, compared to the values of Bushick and Kioupakis at 10^{18} cm^{-3} .

We next develop a parameterisation for the temperature dependence of the Coulomb enhancement factors for the *eeh* and *ehh* processes in the low-concentration limit, based on the above model for C_{n0} and C_{p0} and our own data for C_{amb} at low concentrations. The latter is related to the former according to:

$$C_{amb} = C_n + C_p = g_{eeh} C_{n0} + g_{ehh} C_{p0} \quad (11)$$

where g_{eeh} and g_{ehh} are the Coulomb enhancement factors, and all terms are temperature-dependent. We assume an identical temperature dependence of the Coulomb enhancement term for both *eeh* and *ehh* processes, with the exception of a scalar weighting factor which is constrained to recover the experimental value of Nieuwelt et al. of $C_n/C_p = 2.616$ at 300 K. This necessarily results in a Coulomb enhancement term which is 10 % smaller for the *eeh* process than for the *ehh* process. We find that our measured data for C_{amb} can be well-described using empirical expressions for g_{eeh} and g_{ehh} similar to that used in Eq. (6), with the omission of the final linear term:

$$g_{max,exh} = g_{max,exh,\infty} \left\{ 1 + A \exp \left[- \left(\frac{T}{T_{ref}} \right)^\alpha \right] \right\} \quad (12)$$

where the subscript max indicates that this represents the upper limit obtaining at low carrier concentrations, in anticipation of the introduction of a carrier-concentration dependence below, $g_{max,exh,\infty}$ is the limiting value at high temperatures, A is a proportionality factor, T_{ref} a reference temperature and α an exponent. Using this expression together with Eqs. (7)–(11) and the parameters given in Table 1, we obtain similarly good agreement with measured $C_{amb}(T)$ as with Eq. (6).

In order to account for the transition between the Coulomb-enhanced and screened Auger coefficients with increasing carrier concentration, we parameterise the carrier concentration dependence of g_{eeh} and g_{ehh} in the same manner as both Black and Macdonald and Nieuwelt et al.:

$$g_{exh} = 1 + (g_{max,exh} - 1) \left(1 + \left[\frac{p+n}{N_{ref,exh}} \right]^{\theta_{exh}} \right)^{-1} \quad (13)$$

In this case, we adopt the values of Nieuwelt et al. for $N_{ref,eeh}$, $N_{ref,ehh}$, θ_{eeh} and θ_{ehh} at 300 K, in order to maintain full compatibility with the latter model.

Table 1

Parameter values for use in Eqs. (7)–(14), determined based on our data for $C_{amb}(T)$ together with the temperature dependence of the screened Auger coefficients given by Bushick and Kioupakis [30], with the high-concentration values given by Niewelt et al. [3].

Parameter	Value	Units
$C_{0,eeh,dir}$	1.02×10^{-31}	$\text{cm}^6 \text{s}^{-1}$
$E_{a,eeh}$	2.8	meV
$C_{0,ehh,pa}$	9.71×10^{-32}	$\text{cm}^6 \text{s}^{-1}$
$\hbar\omega_{eeh}$	21.2	meV
$C_{0,ehh,pa}$	4.51×10^{-32}	$\text{cm}^6 \text{s}^{-1}$
$\hbar\omega_{ehh}$	21.0	meV
$g_{max,eeh,\infty}$	1.629	–
$g_{max,ehh,\infty}$	1.815	–
A	880.9	–
T_{ref}	17.51	K
α	0.6434	–
$N_{ref,eeh,300K}$	4×10^{17}	cm^{-3}
$N_{ref,ehh,300K}$	4×10^{17}	cm^{-3}
θ_{eeh}	2	–
θ_{ehh}	2	–
β	4	–

In principle, the threshold concentrations for the screening transition, $N_{ref,eeh}$ and $N_{ref,ehh}$ should also be a function of temperature. There is limited experimental and theoretical work available to guide a description of this dependence. The only previous complete temperature-dependent parameterisation of Auger recombination, by Altermatt et al. [11], did not include a temperature dependence for the threshold concentrations. Nevertheless, such a temperature dependence of the threshold concentrations is known to obtain in the case of the two-particle electron–hole Coulomb-enhancement term g_{eh} (i.e. as relevant for radiative recombination), based on experimental evidence as well as theoretical calculations [31,40]. Hangleiter and Häcker [41] have argued that g_{eeh} and g_{ehh} should be given to a first approximation by the product of the two-particle correlation factors (i.e. $g_{eeh} = g_{eh}^2 \times g_{ee}$ and $g_{ehh} = g_{eh}^2 \times g_{hh}$, where g_{ee} and g_{hh} are the electron–electron and hole–hole correlation factors). Consequently, the former should display a similar functional dependence on temperature when it comes to the threshold concentrations for screening. Altermatt et al. [40] parameterised their results for the theoretical temperature and concentration dependence of g_{eh} using a generalised (five-parameter) logistic function, with a concentration threshold that varies approximately as $\sim T^{2.88}$ over the relevant temperature range. Recently, it has been argued that Altermatt et al.’s model for g_{eh} should in fact be interpreted as a parameterisation of bandgap narrowing, specifically of $\exp(-\Delta E_g/kT)$, where ΔE_g is the bandgap reduction due to bandgap narrowing [42]. Schenk’s theoretical bandgap narrowing model gives a temperature-dependence for the threshold concentration of this quantity that varies as $\sim T^{3.98}$. We further note that this temperature dependence is similar to that for the onset of significant carrier–carrier scattering (relative to lattice scattering) in the mobility models of Dorkel and Leturcq [43] ($\sim T^{3.64}$) and Klaassen ($\sim T^{4.15}$). This is likely not coincidental since the correlation factors also involve a scattering state component [41], while the total screening effect is expected to be a function of the sum of lattice and free-carrier contributions to the dielectric constant [44].

Based on the above considerations, we tentatively identify a T^4 dependence as a reasonable approximation of the likely temperature dependence of $N_{ref,eeh}$ and $N_{ref,ehh}$. We then have

$$N_{ref,exh} = N_{ref,exh,300K} \left(\frac{T}{300} \right)^\beta \quad (14)$$

with $\beta = 4$. Combining Eqs. (7)–(14), we now have a complete description of the Auger recombination rate as a function of temperature and carrier concentration. These equations are summarised in Table 2 and their parameter values are summarised in Table 1.

6. Evaluation of model predictions

It is important to compare the predictions of the developed model against other available data to check for possible inconsistencies. Fig. 4 plots $C_{amb}(\Delta n, T)$ given by Eqs. (7)–(14) as a function of temperature for a range of values of Δn . It can be seen that for certain values of Δn in the intermediate carrier concentration range, the model predicts a non-monotonic behaviour for $C_{amb}(T)$, with a peak value occurring at some well-defined temperature. Our own data does not allow us to test this prediction directly, because the maximum measurable carrier concentration in the relevant temperature range was below this threshold. Instead we compare our model to the data of Jonsson et al. which was measured in the intermediate injection range ($\Delta n \approx 1 \times 10^{17} \text{ cm}^{-3}$ to $3 \times 10^{17} \text{ cm}^{-3}$). For comparison purposes, we scale the data of Jonsson et al. by a factor of 0.67 to better highlight the comparison with our model (such an adjustment could correspond e.g. to a 18% underestimation of the carrier concentration in the measurements of Jonsson et al.). As is apparent from Fig. 4, our model is able to describe the temperature dependence of the data reasonably well if an injection level in the range of $\sim 3 \times 10^{17} \text{ cm}^{-3}$ is assumed, consistent with the reported experimental conditions of Jonsson et al. While we would caution against over-interpretation of this agreement given the somewhat problematic nature of the aforementioned data (as discussed above), the apparent consistency between our model and the limited available data in this range is at least reassuring.

7. Sources of uncertainty

A significant source of uncertainty in the extracted C_{amb} is the choice of mobility model used to calculate $\Delta n(t)$ from the measured photoconductance decay data. As discussed in our previous work, existing mobility models are subject to significant uncertainty regarding their injection dependence even at room temperature [2]. Greater uncertainty attaches to the injection dependence at temperatures far from room temperature, and particularly at low temperatures, where this dependence becomes quite pronounced, and relatively little experimental data is available.

In order to assess the influence of the choice of mobility model, we also analysed the experimental data using several alternative temperature-dependent mobility models [43,45–47]. The results are shown in Fig. 5. It can be seen that the influence of the choice of mobility model is greatest at lower temperatures. Here the models of Dorkel and Leturcq and Zheng et al. result in significantly lower and higher values of C_{amb} , respectively, while that of Schindler et al. results in only slightly higher values. At 300 K, there is good agreement between the values produced by all models except for that of Dorkel and Leturcq, which results in somewhat lower values. At high temperatures all models converge to similar values, so that relatively little uncertainty results from the choice of mobility model in this range. It should be noted that in all cases we have used the same temperature-dependent coil calibration coefficients, which were determined by using the model of Klaassen to calculate the expected change in equilibrium mobility for the calibration samples. For full self-consistency we should strictly also use these models when calibrating the coil. In all cases this would tend to reduce the deviation of the extracted values from those calculated using the Klaassen mobility. In other words, potential errors in the equilibrium component of the mobility model are to some extent compensated by the calibration process.

Another potential source of uncertainty is the influence on the measurements of edge recombination, which is known to be present in these samples (due to post-passivation cleaving) but was not explicitly accounted for in the analysis. However, our separate quantitative assessment of this factor (Appendix C) indicates that its influence on the extracted C_{amb} values is small.

Table 2
Summary of equations for the temperature dependence of the Auger coefficients.

Fit type	Equation
Empirical (Eq. (6))	$C_{amb} = 2.290 \times 10^{-31} \left\{ 1 + 811.7 \exp \left[- \left(\frac{T}{18.17} \right)^{0.6498} \right] \right\} \left(1 + \frac{T}{122.6} \right)$
Semi-empirical (Eqs. (7)–(14))	$C_{eeh,dir} = C_{0,eeh,dir} \exp \left(- \frac{E_{a,eeh}}{kT} \right)$ $C_{exh,pa} = C_{0,exh,pa} \left\{ 1 + 2 \left[\exp \left(\frac{\hbar\omega_{exh}}{kT} \right) - 1 \right]^{-1} \right\}$ $C_{n0} = C_{eeh,dir} + C_{eeh,pa}$ $C_{p0} = C_{exh,pa}$ $g_{max,exh} = g_{max,exh,\infty} \left\{ 1 + A \left[- \left(\frac{T}{T_{ref}} \right)^a \right] \right\}$ $N_{ref,exh} = N_{ref,exh,300K} \left(\frac{T}{300} \right)^\beta$ $g_{exh} = 1 + (g_{max,exh} - 1) \left(1 + \left[\frac{p+n}{N_{ref,exh}} \right]^{\theta_{exh}} \right)^{-1}$ $C_n = g_{eeh} C_{n0}$ $C_p = g_{exh} C_{p0}$

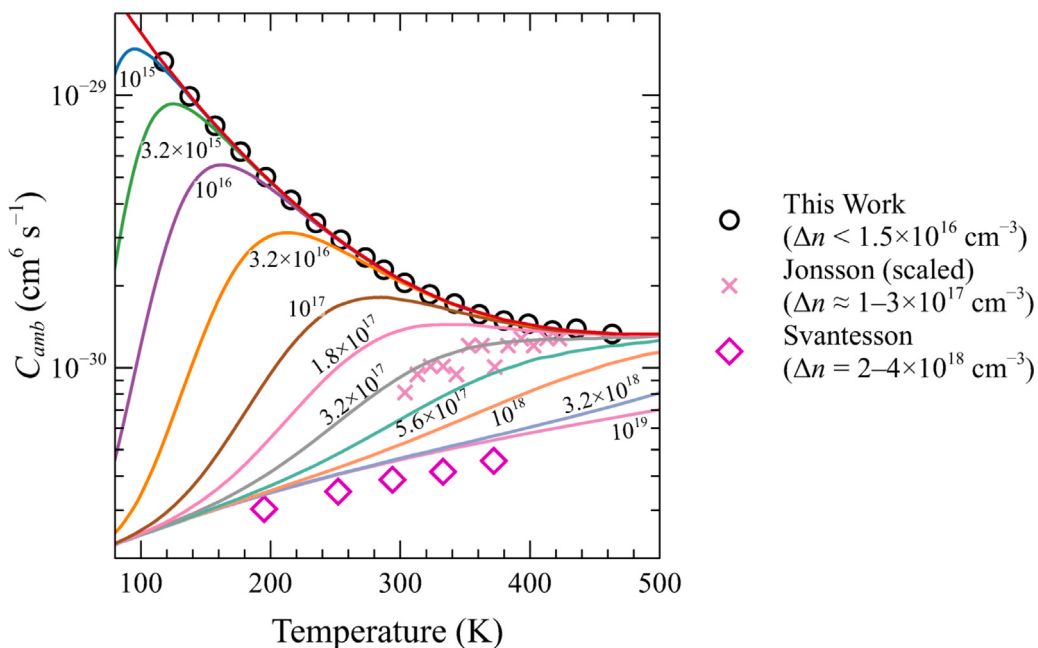


Fig. 4. C_{amb} vs temperature with Δn as a parameter, calculated from Eqs. (7)–(14) (lines). Labels indicate corresponding values of Δn . The data of Jonsson et al., which were extracted based on measurements performed at $\Delta n \approx 1 \times 10^{17} \text{ cm}^{-3}$ to $3 \times 10^{17} \text{ cm}^{-3}$, are shown for comparison, along with the data of Svantesson and Nilsson, which were measured at $\Delta n \approx 2 \times 10^{18} \text{ cm}^{-3}$ to $4 \times 10^{18} \text{ cm}^{-3}$. We have scaled the values of Jonsson et al. by a factor of 0.67 to highlight the comparison with the temperature dependence predicted by our model.

8. Comparison to previous parameterisations

Fig. 6 compares the parameterisations of $C_{amb}(T)$ described by (i) Eq. (6) and (ii) Eqs. (7)–(14) to the previous parameterisations of Altermatt et al., Wang and Macdonald, and Bushick and Kioupakis. Here we include a wider temperature range extending outside the range of measured data in order to compare the behaviour of these parameterisations when extrapolated beyond this range.

As a first remark, it can be seen that there is virtually no difference between the values predicted by Eq. (6) and Eqs. (7)–(14) (with the latter in this case evaluated at low carrier concentrations), except for a very slight deviation at the lowest temperatures below 100 K ($\sim 3.5\%$ at 77 K). Agreement is better than 1% between 112 K and 830 K. Hence, these parameterisations can be considered equivalent for $C_{amb}(T)$ in the unscreened (low concentration) limit. Furthermore, from comparison between Eq. (6) and Eqs. (7)–(14), it can be seen that the origin of the linear term in (6), which is absent in (12), is the temperature dependence of the phonon absorption/emission terms which dominate the

screened process, as described by Eqs. (7)–(10), which is approximately linear in the examined temperature range.

Despite the fact that the parameterisation of Altermatt et al. [11] predicts much higher values for C_{amb} than ours due to being based on measurements of extrinsically-limited samples, it is interesting to note that it predicts a qualitatively similar relative temperature trend to our model between ~ 300 K to 400 K. However, it diverges at higher temperatures, predicting a continued decrease of C_{amb} where our model predicts a saturation followed by a gradual increase. This is clearly, at least partly, a consequence of the simple power dependence used to describe the Coulomb-enhancement factors in the parameterisation of Altermatt et al., as well as the more limited temperature range of the underlying data of Häcker and Hangleiter (which only extended to 360 K). Altermatt et al.'s parameterisation also predicts a somewhat slower relative rise of C_{amb} with reducing temperature below 300 K.

Unlike the parameterisation of Wang and Macdonald [12], which diverges rapidly at temperatures below the range of measured data (< 243 K) and is undefined or negative for $T \leq 193$ K, the developed

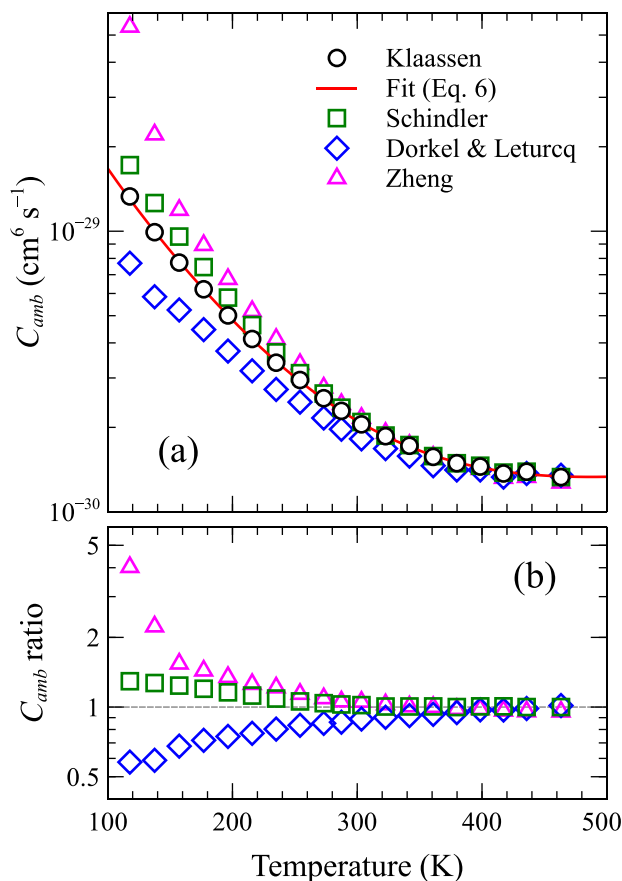


Fig. 5. (a) Influence of the choice of mobility model on calculated C_{amb} vs temperature. (b) Corresponding ratio of C_{amb} for each model to that determined using the mobility model of Klaassen et al.

model is numerically well-behaved, and can be reasonably extrapolated to both lower and higher temperatures beyond the measured range. Despite their different functional forms, at higher temperatures both parameterisations predict a very similar dependence of C_{amb} on temperature, converging to a slope that parallels that of the screened dependence predicted by Bushick and Kioupakis.

9. Consequences for devices

The temperature dependence of Auger recombination affects the theoretical efficiency limit for photovoltaic devices operating near the Auger limit at temperatures away from room temperature. We have evaluated the theoretical limiting efficiency (i.e. for an Auger-limited device with Lambertian light-trapping) as a function of temperature using both the Auger model of this work and the temperature-independent model of Niewelt et al. In Fig. 7 we plot the ratio of the resulting values for open-circuit voltage (V_{oc}), fill factor (FF) and output power (P_{out}), as well as the absolute difference in efficiency η , as a function of temperature. From this we can see that consideration of the temperature dependence of the Auger recombination will, for example, increase the theoretical efficiency limit for a device operating at 65 °C by a factor of 0.14 % absolute, or over 0.5 % relative, which could be significant for yield calculations of systems operating in warmer climates.

The variation of device operating characteristics with temperature is often quantified in terms of temperature coefficients for the short-circuit current J_{sc} , open-circuit voltage V_{oc} , fill factor FF , and output power P_{out} . For devices operating near the Auger limit, the temperature

dependence of Auger recombination will affect these temperature coefficients. We calculate that incorporating the temperature-dependence of Auger recombination given by our model will decrease the absolute temperature coefficient of P_{out} at 25 °C by a factor of 0.015 °C⁻¹ for an Auger-limited device (e.g. from -0.284 °C⁻¹ to -0.269 °C⁻¹ for an absorber thickness of 100 μm), compared to calculations ignoring this temperature dependence (using the model of Niewelt et al.). This is primarily due to a 0.012 °C⁻¹ reduction in the absolute temperature coefficient of V_{oc} , as well as a smaller 0.003 °C⁻¹ reduction in the absolute temperature coefficient of the FF , as reflected in Fig. 7a.

10. Future work

The model of Bushick and Kioupakis predicts an additional concentration dependence (specifically a reduction) of the Auger coefficients at very high carrier concentrations ($>10^{18} \text{ cm}^{-3}$), due to screening of long-range Coulomb interactions involved in the phonon-assisted processes. This effect is distinct from the spatial correlation effects (Coulomb-enhancement) which obtain at lower concentrations, which Bushick and Kioupakis explicitly do not consider in their model. This may explain earlier seemingly anomalous experimental results which also showed a reduction of the Auger coefficients in this range [48,49]. We have neglected this component in developing the model presented in the current work, in order to maintain consistency with the established model of Niewelt et al. at higher concentrations, which assumes convergence to a constant value. There may however be grounds for reconsidering the model at higher concentrations in light of these theoretical results as well as recent experimental measurements of the Auger lifetimes at high concentrations [50], which appear to support earlier works which showed such a dependence. Consideration of this factor would not alter the parameterisation of Auger recombination at low carrier concentrations, but could have some influence on model predictions in the transitional concentration range. It is mainly relevant for calculations of Auger recombination in highly doped surface regions such as those present in homojunction devices.

Limited experimental data is currently available to support or refute model predictions within the transitional carrier concentration range (as embodied by Eqs. (13) and (14)). Additional experimental data to test model predictions in this range would be welcome. Measurements in this range are however inherently challenging for multiple reasons. For measurements relying on photoionization of carriers, achieving carrier concentrations in the relevant range (e.g. $\gtrsim 10^{17} \text{ cm}^{-3}$ at room temperature) requires very high levels of excitation that are difficult to realise experimentally. Furthermore, measurement of such large excited carrier concentrations depends on physical models for quantities such as mobility, radiative coefficient, or bandgap narrowing that are themselves subject to significant uncertainty in the relevant carrier concentration range [2]. Obviously, such high levels of excitation can also lead to challenges with effective temperature control. An alternative could be to investigate the temperature-dependence of the low-injection lifetime in moderately doped material ($\sim 10^{17} \text{ cm}^{-3}$ to 10^{18} cm^{-3}). However, this comes with its own challenges. For instance, the influence of surface recombination is challenging to eliminate at such surface dopant concentrations, and must somehow be accounted for. Partial ionisation of dopants is also expected to be significant at such concentrations and must be considered, as this can be expected to significantly alter the observed temperature dependence.

11. Conclusion

We have measured the ambipolar Auger coefficient C_{amb} in crystalline silicon as a function of temperature from 117 K to 463 K. Our measurements are in excellent agreement with the recent parameterisation of Niewelt et al. near room temperature. They confirm that C_{amb} increases strongly at lower temperatures, and decreases significantly at temperatures above room temperature, in the range relevant for solar

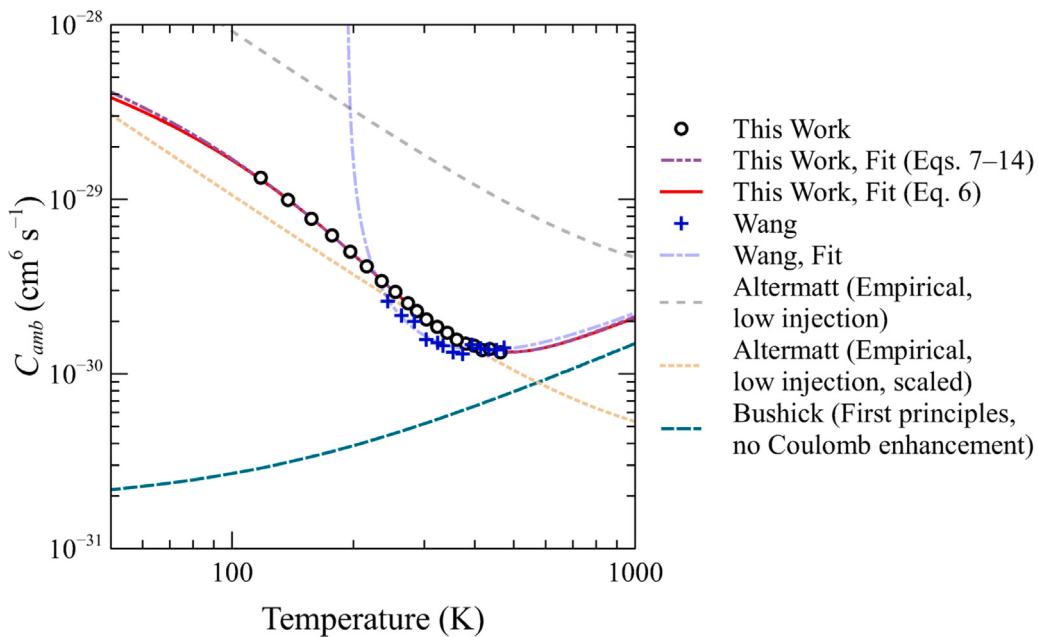


Fig. 6. Comparison of Eq. (6) and Eqs. (7)–(14) with previous parameterisations of C_{amb} vs temperature.

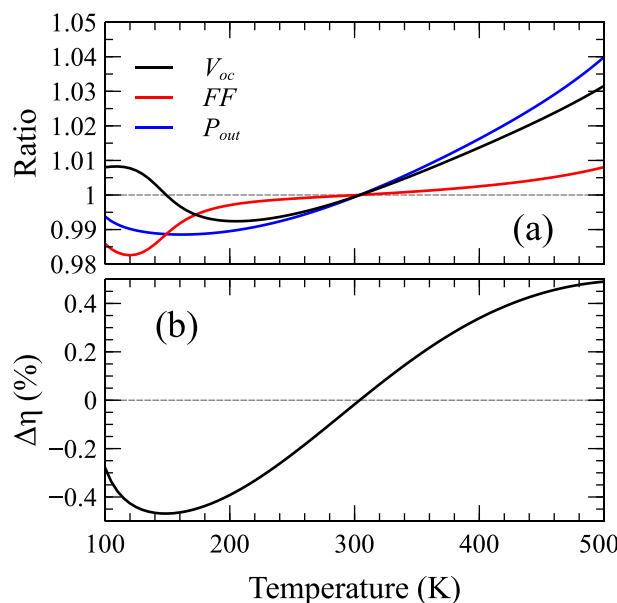


Fig. 7. (a) Ratio of V_{oc} , FF , and P_{out} at the theoretical efficiency limit when using the Auger model of this work, compared to that calculated using the temperature-independent model of Niewelt et al. and (b) corresponding difference in absolute conversion efficiency η , as a function of temperature.

cell operation. This can be understood in terms of the temperature dependence of the Coulomb enhancement factors. We have proposed a semi-empirical parameterisation which extends the currently accepted model of Niewelt et al. for Auger recombination near room-temperature to incorporate the observed temperature dependence. The resulting model is valid over a wide temperature range and for arbitrary carrier concentrations. Consideration of the temperature dependence of Auger recombination has significant consequences for the expected performance of Auger-limited solar cells operating at temperatures commonly seen by photovoltaic modules in the field.

CRediT authorship contribution statement

Lachlan E. Black: Writing – original draft, Visualization, Software, Methodology, Investigation, Funding acquisition, Formal analysis, Conceptualization. **Yan Zhu:** Writing – review & editing, Software, Methodology, Investigation, Funding acquisition. **Ziv Hameiri:** Writing – review & editing, Supervision, Resources, Funding acquisition. **Daniel H. Macdonald:** Writing – review & editing, Supervision, Funding acquisition.

Declaration of competing interest

The authors declare the following financial interests/personal relationships which may be considered as potential competing interests: Lachlan E. Black reports financial support was provided by Australian Renewable Energy Agency. Lachlan E. Black reports financial support was provided by Australian Centre for Advanced Photovoltaics. If there are other authors, they declare that they have no known competing financial interests or personal relationships that could have appeared to influence the work reported in this paper.

Acknowledgements

This work was supported by the Australian Centre for Advanced Photovoltaics (ACAP) and received funding from the Australian Renewable Energy Agency (ARENA; 2022/TRAC001). The authors acknowledge Marco Ernst and Roel J. Theeuwes for assistance with sample preparation.

Appendix A. Calibration procedure

The actual sample temperature corresponding to a given set-point temperature was calibrated using a dedicated calibration sample, consisting of a silicon wafer with two thermocouples (Omega k-type, model CHAL-005) attached by polyimide adhesive tape (Kapton). The thermocouple wires were sufficiently thin to allow them to pass through the gap between the cryostat base and cover while the cryostat was closed. The sample temperature measured by each thermocouple, as well as the stage temperature, were recorded as a function of time, and allowed to stabilise for at least 1 h following each set-point temperature step.

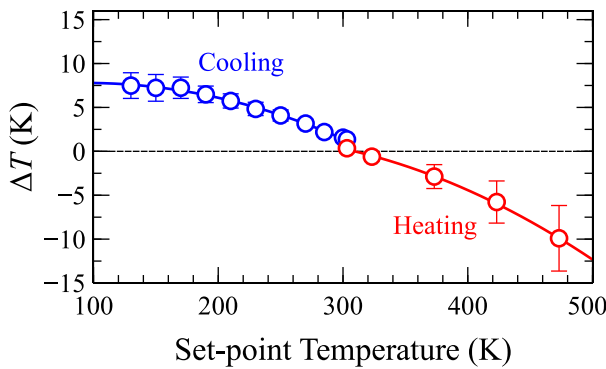


Fig. A.8. Difference between measured sample temperature and set-point temperature as a function of the latter. Error bars show the upper and lower values measured by the two thermocouples. Lines show polynomial fits used to calculate actual temperatures corresponding to set-point values.

Resulting calibration curves of stabilised sample temperature vs set-point temperature were recorded covering the measurement range. Fig. A.8 plots the difference between the sample temperature and set-point temperature as a function of the latter.

For the purposes of subsequent analysis, the actual sample temperature corresponding to a given set-point temperature was taken as the average of the two thermocouple readings. Polynomial fits made to this average value as a function of temperature were used to calculate actual temperatures corresponding to each set-point temperature during the measurements. Separate fits were used for temperatures $\geq 300\text{ K}$ (heating only) and $< 300\text{ K}$ (combined heating and cooling). Unless otherwise mentioned, temperature values mentioned in the text refer to the actual sample temperatures determined by this method, which were used for subsequent analysis.

The relationship between the measured coil voltage and sample conductance was determined using a set of 2 inch diameter silicon wafers of varying conductance, spanning the range measured in the lifetime measurements. The apparent dark conductance of these samples was calibrated against the existing calibration sample set #2 described in [25] using photoconductance system #1 of that work, for which the characteristic attenuation length λ of the coil has been carefully determined previously. The actual dark conductance of each sample at the calibration temperature was calculated from the apparent dark conductance G_{app} according to Eq. 2 of [25]. The corresponding total dopant concentration was subsequently determined by applying the mobility model of [26,27] together with the ionisation model of [51, 52]. This was then used to calculate the expected apparent conductance of the same samples at other temperatures using the same models.

The characteristic attenuation length λ of the measurement system used in the present work was determined in the manner described in [25] from measurements of the calibration sample set at $30\text{ }^\circ\text{C}$, both individually and as pairs of stacked wafers in different configurations. A resulting value of $\lambda = 3.32\text{ mm}$ was obtained by minimising the sum of squares of the relative error between the calculated apparent conductance of the samples and a linear fit vs coil voltage, given by:

$$G_{app} = B_{cal}(V_{dark} - V_{air}) + C_{cal} \quad (\text{A.1})$$

Using the value of λ so determined, the relationship between apparent conductance and measured voltage could be described to within a $< 1\%$ relative error for all samples. The addition of a quadratic term, as commonly found to be necessary to describe such relationships in similar systems, was considered, but the resulting improvement in the fit was found to be negligible, and therefore we chose not to include such a term.

Subsequently, the coil voltage for the same calibration samples was measured at a range of temperatures and used to construct calibration

curves at those temperatures (see Fig. A.9). Similarly to the temperature calibration, samples were allowed to stabilise for at least 1 h following each set-point temperature step. At higher temperatures (heating only), use of the value of λ obtained at $30\text{ }^\circ\text{C}$ was found to result in good linear characteristics for all samples, including both single and stacked samples. Meanwhile, at lower temperatures (cooling plus heating), it was found that results obtained for stacked samples could only be explained by assuming that the top sample in the stack was at a higher temperature than the bottom sample (the sample in contact with the stage), indicating non-uniform temperature between the samples. Therefore, we chose to neglect data for stacked samples at lower temperatures, and to assume λ to be independent of temperature. Note that the latter assumption is supported by the results of electromagnetic simulations performed using the Finite Element Method Magnetics software [53] (not shown), which do not predict a significant temperature dependence of λ (which is essentially a geometrical factor) for such systems.

The resulting values of the calibration coefficients B_{cal} and C_{cal} as a function of temperature are shown in Fig. A.10. Similar to the temperature calibration, these clearly form two discontinuous series of data: one for temperatures $\geq 300\text{ K}$ (heating only) and one for temperatures $< 300\text{ K}$ (combined heating and cooling). The discontinuity between these series may be attributed to the fact that the relationship between a given sample temperature and the temperature of other components in the measurement system is different in each case. We found the temperature dependence of B_{cal} and C_{cal} in each series to be well described by quadratic and linear fits respectively. These fits were then used to calculate B_{cal} and C_{cal} at other sample temperatures.

Appendix B. C_{amb} extraction data summary

Fig. B.11 shows the C_{amb} extraction plots for all measurement temperatures.

Appendix C. Influence of edge recombination

Since the sample was cleaved subsequent to passivation (in order to fit within the cryostat sample stage), it can be expected that significant edge recombination will be present, and therefore its influence on the measurements and extraction of C_{amb} should be assessed. Photoluminescence imaging of the sample at room temperature under varying excitation intensity after cleaving showed clear evidence of edge recombination at the edge that was cleaved post-passivation. In order to quantify this effect, steady-state PL intensity was calibrated to Δn in the manner described in our previous work [23], after first deconvolving the raw PL image to correct for smearing of the PL signal [23]. The resulting non-uniformity of Δn was assessed over the area probed in the photoconductance lifetime measurements (2.5 cm diameter, as defined by the size of the cavity surrounding the inductive coil within the cryostat [25]). This analysis revealed a relative standard deviation of $\sim 3.2\%$ in Δn over the measurement area at 0.5 Suns, and $\sim 7.8\%$ at 0.05 Suns. Note that these excitation intensities correspond to average excess carrier concentrations of $\sim 8.7 \times 10^{15}\text{ cm}^{-3}$ and $\sim 2.6 \times 10^{15}\text{ cm}^{-3}$ respectively, which closely matches the range used for extraction of C_{amb} at 303.4 K .

In order to assess the influence of lateral non-uniformity due to edge recombination under transient excitation conditions (as used in the actual lifetime measurements), and at other temperatures, we make use of the following observations:

- Under steady-state excitation conditions, the measured carrier profile close to the edge is well-described by the well-known solution of the steady-state continuity equation for diffusion towards an infinitely recombinative surface under conditions of uniform generation:

$$\Delta n(x) = \Delta n_\infty \left[1 - \exp \left(\frac{-x}{\sqrt{D\tau}} \right) \right] \quad (\text{C.1})$$

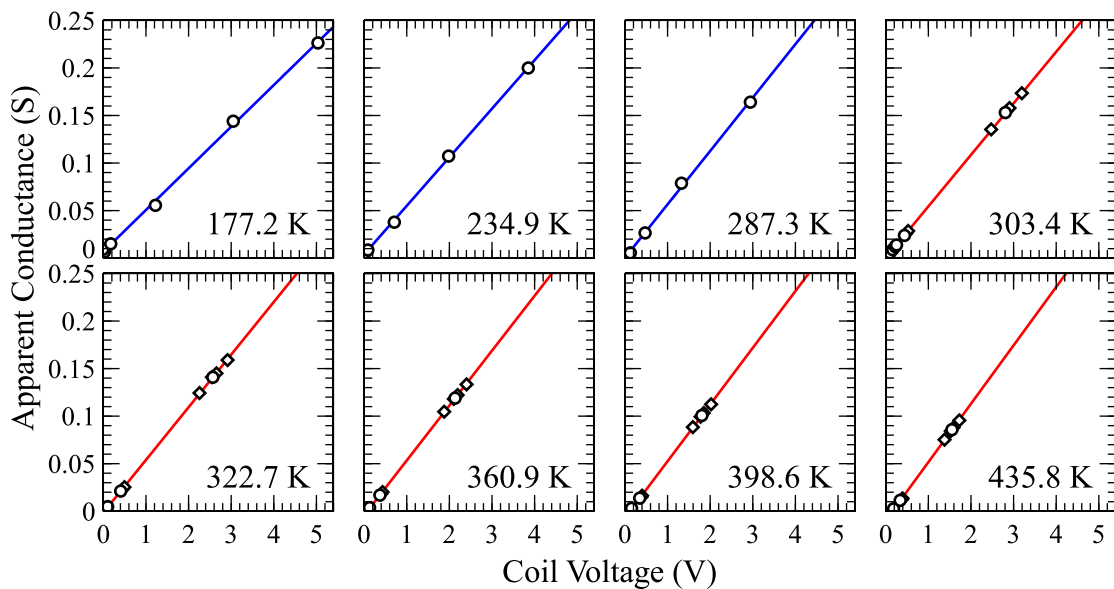


Fig. A.9. Calibration curves of apparent sample conductance vs coil voltage measured for calibration samples in the dark at various sample temperatures. Circles indicate single samples, while diamonds indicate stacked pairs of samples. Lines show linear fits to the data used for determining the calibration coefficients.

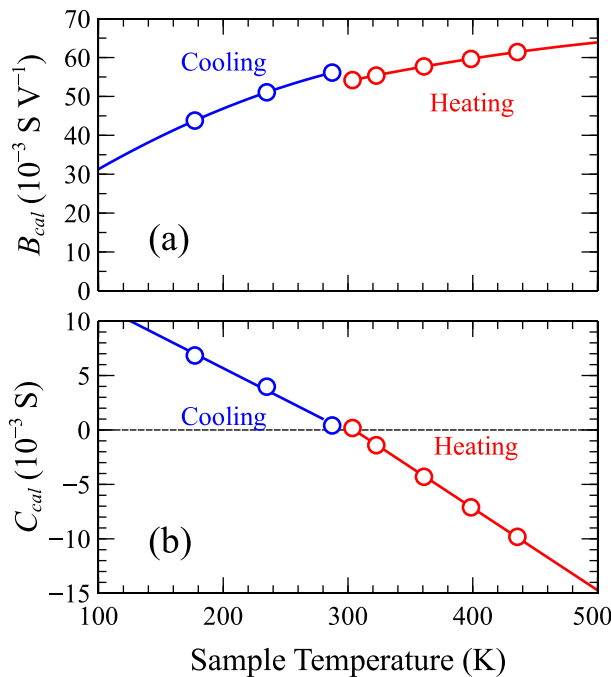


Fig. A.10. Calibration coefficients (a) B_{cal} and (b) C_{cal} for the photoconductance coil as a function of sample temperature. Lines show quadratic (for B_{cal}) and linear (for C_{cal}) fits used to calculate calibration coefficients at other sample temperatures.

where x is the distance from the edge, Δn_∞ is the value of Δn far from the edge, D is the diffusion coefficient and τ the carrier lifetime.

2. Specifically, we obtain reasonable fits of (C.1) to the measured $\Delta n(x)$ profile by setting D equal to the ambipolar diffusion coefficient (D_{amb}) corresponding to the mean Δn and τ equal to mean τ_{eff} within the measurement area.
3. Evaluation of the relative standard deviation of Δn over either the experimental $\Delta n(x)$ profile, or that described by (C.1), within

the bounds of the measurement area, yields similar values to those obtained from the full measurement area.

Based on the above, we conclude that (i) the edge recombination is diffusion-limited, and (ii) we can make a reasonable estimate of the error in $\tau_{eff}^{-1}(\Delta n)$ due to edge recombination, given knowledge of $\Delta n(x)$ near the edge.

For transient excitation conditions, $\Delta n(x, t)$ for time t after the excitation pulse should be given by another well-known solution of the continuity equations:

$$\Delta n(x, t) = \Delta n(t=0) \operatorname{erf} \left(\frac{x}{2\sqrt{Dt}} \right) \exp(-t/\tau) \quad (\text{C.2})$$

Note that the derivation (C.2) assumes D and τ are independent of time and therefore of Δn . Although this is not actually the case, the variation of D with Δn is fairly minor, while the variation of τ with Δn only affects the magnitude of the profile and not its shape.

For each measurement temperature, we determine the range of decay times t corresponding to the Δn range that was used to extract C_{amb} from the transient photoconductance measurement data, and calculate the corresponding range of Dt using the theoretical ambipolar diffusion coefficient at that temperature. We then calculate $\Delta n(x, t)$ across this range using (C.2), and use this to calculate $\tau_{eff}^{-1}(x, t)$, using the values for C_{amb} , B and τ_{SRH} obtained from our analysis of the lifetime data. We then assess the mean values of Δn and the recombination rate $\tau_{eff}^{-1}\Delta n$ over the measurement area at each time t , and compare the latter to $\tau_{eff}^{-1}\Delta n$ calculated from the mean Δn . In the most extreme case (which occurs at 254.1 K), this results in an error (specifically an underestimation) of 0.1%–2.1% in $\tau_{eff}^{-1}(\Delta n)$ over the C_{amb} extraction range. At other temperatures, the resulting error is smaller, either because Dt is smaller, or because τ_{eff}^{-1} varies less steeply with Δn in the relevant range. Although Dt obviously increases at longer decay times and therefore at lower Δn , we do not expect the error in $\tau_{eff}^{-1}(\Delta n)$ to increase significantly in this range because (i) the shape of the carrier profile can be expected to reach a steady state at longer decay times and (ii) τ_{eff}^{-1} varies less with Δn as Δn decreases. Therefore, we consider that the effect of this non-uniformity on the extraction of C_{amb} can reasonably be neglected.

Separate from its influence on lateral non-uniformity, edge recombination also obviously influences the measured lifetime by increasing total recombination. Indeed, we observe a reduction in the measured

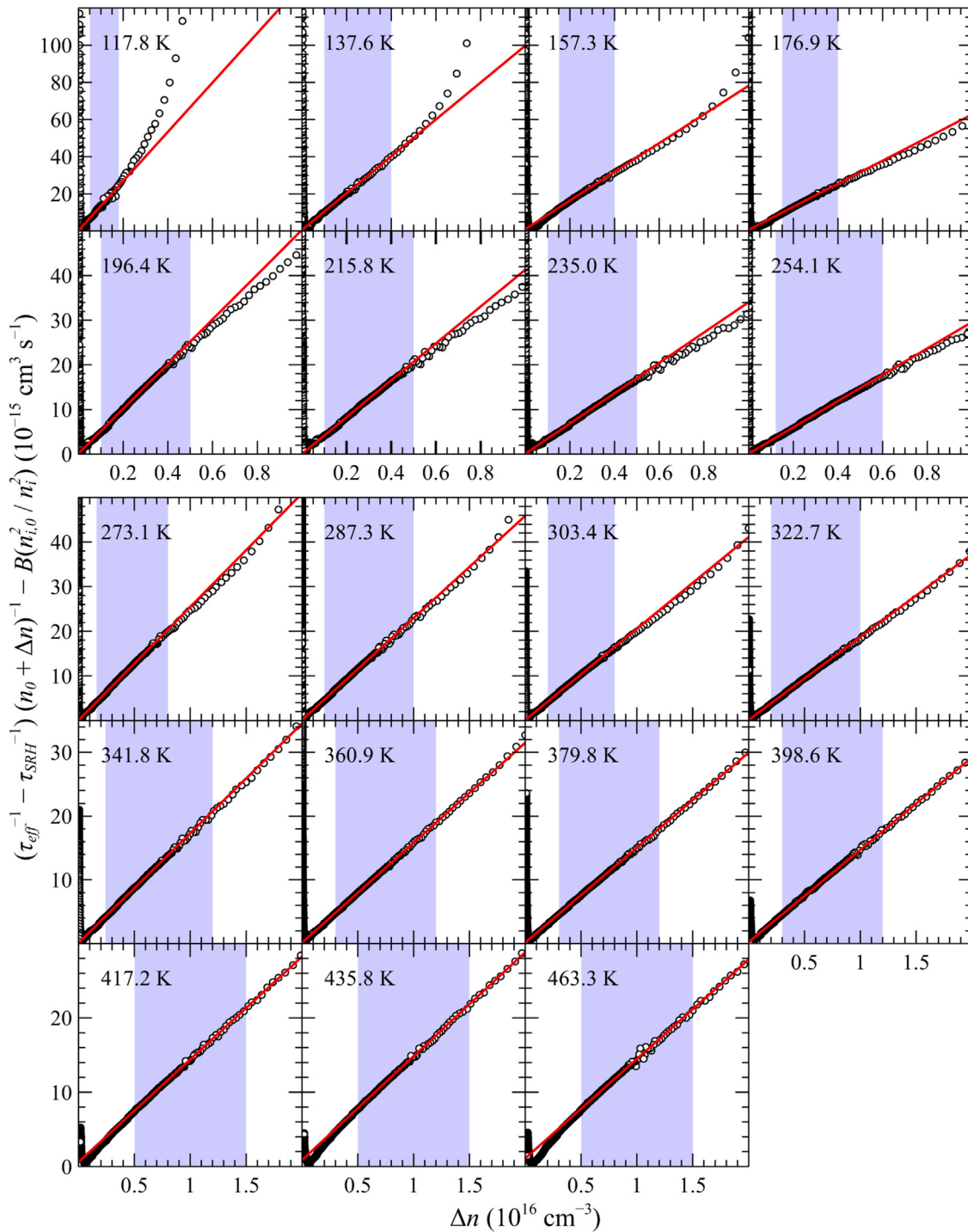


Fig. B.11. Summary of C_{amb} extraction via (4) for all measurement temperatures. Data points show measurement data after correction for bulk SRH and surface recombination, while solid lines show linear fits to determine C_{amb} from the slope. The blue shaded region indicates the carrier concentration range used to fit C_{amb} at each temperature. Note the different y axis ranges used for each row of subfigures, and the change in the carrier concentration range between the lower and higher temperatures.

lifetime at room temperature following cleaving. A particular concern in the present case is how this might affect the extraction of C_{amb} via (4). We do not account explicitly for edge recombination in (4). However, in the case of an unpassivated edge (very high surface recombination velocity), edge recombination is expected to contribute a lifetime component $\tau_{edge}^{-1} \propto D_{amb}$, analogous to the case of an unpassivated surface [54]. Such an injection dependence can be described to a good approximation using the $\tau_{SRH}^{-1}(n_0 - \Delta n)$ term in (4). Therefore,

we consider that the edge recombination contribution is effectively absorbed in τ_{SRH} , and likely does not strongly influence the extracted values of C_{amb} .

Data availability

Data will be made available on request.

References

- [1] D. Matsakis, A. Coster, B. Laster, R. Sime, A renaming proposal: “The Auger–Meitner effect”, *Phys. Today* 72 (9) (2019) 10–11.
- [2] L.E. Black, D.H. Macdonald, On the quantification of Auger recombination in crystalline silicon, *Sol. Energy Mater. Sol. Cells* 234 (2022) 111428.
- [3] T. Niewelt, B. Steinhauser, A. Richter, B. Veith-Wolf, A. Fell, N.E. Grant, L.E. Black, J.D. Murphy, M.C. Schubert, S.W. Glunz, Reassessment of the intrinsic bulk recombination in crystalline silicon, *Sol. Energy Mater. Sol. Cells* 235C (2022) 111467.
- [4] H. Lin, M. Yang, X. Ru, G. Wang, S. Yin, F. Peng, C. Hong, M. Qu, J. Lu, L. Fang, C. Han, P. Procel, O. Isabella, P. Gao, Z. Li, X. Xu, Silicon heterojunction solar cells with up to 26.81% efficiency achieved by electrically optimized nanocrystalline-silicon hole contact layers, *Nat. Energy* 8 (8) (2023) 789–799.
- [5] M.D. Kempe, D. Holsapple, K. Whitfield, N. Shiradkar, Standards development for modules in high temperature micro-environments, *Prog. Photovolt., Res. Appl.* 29 (4) (2021) 445–460.
- [6] C. Buttay, D. Planson, B. Allard, D. Bergogne, P. Bevilacqua, C. Joubert, M. Lazar, C. Martin, H. Morel, D. Tournier, C. Raynaud, State of the art of high temperature power electronics, *Mater. Sci. Eng.: B* 176 (4) (2011) 283–288.
- [7] S. Nie, R.S. Bonilla, Z. Hameiri, Unravelling the silicon-silicon dioxide interface under different operating conditions, *Sol. Energy Mater. Sol. Cells* 224 (2021) 111021.
- [8] J. Dziewior, W. Schmid, Auger coefficients for highly doped and highly excited silicon, *Appl. Phys. Lett.* 31 (5) (1977) 346–348.
- [9] K.G. Svantesson, N.G. Nilsson, The temperature dependence of the Auger recombination coefficient of undoped silicon, *J. Phys. C: Solid State Phys.* 12 (23) (1979-12) 5111.
- [10] P. Jonsson, H. Bleichner, M. Isberg, E. Nordlander, The ambipolar Auger coefficient: Measured temperature dependence in electron irradiated and highly injected n-type silicon, *J. Appl. Phys.* 81 (5) (1997) 2256–2262.
- [11] P.P. Altermatt, J. Schmidt, G. Heiser, A.G. Aberle, Assessment and parameterisation of Coulomb-enhanced Auger recombination coefficients in lowly injected crystalline silicon, *J. Appl. Phys.* 82 (10) (1997) 4938–4944.
- [12] S. Wang, D. Macdonald, Temperature dependence of Auger recombination in highly injected crystalline silicon, *J. Appl. Phys.* 112 (11) (2012-12) 113708.
- [13] R.F. Häcker, (Ph.D. thesis), University of Stuttgart, 1991.
- [14] R. Häcker, A. Hangleiter, Intrinsic upper limits of the carrier lifetime in silicon, *J. Appl. Phys.* 75 (11) (1994) 7570–7572.
- [15] M.J. Kerr, A. Cuevas, General parameterization of Auger recombination in crystalline silicon, *J. Appl. Phys.* 91 (4) (2002) 2473–2480.
- [16] A. Richter, S.W. Glunz, F. Werner, J. Schmidt, A. Cuevas, Improved quantitative description of Auger recombination in crystalline silicon, *Phys. Rev. B* 86 (2012).
- [17] B.A. Veith-Wolf, S. Schäfer, R. Brendel, J. Schmidt, Reassessment of intrinsic lifetime limit in n-type crystalline silicon and implication on maximum solar cell efficiency, *Sol. Energy Mater. Sol. Cells* 186 (2018) 194–199.
- [18] K.R. McIntosh, L.E. Black, On effective surface recombination parameters, *J. Appl. Phys.* 116 (1) (2014).
- [19] N.E. Grant, V.P. Markevich, J. Mullins, A.R. Peaker, F. Rougier, D. Macdonald, Thermal activation and deactivation of grown-in defects limiting the lifetime of float-zone silicon, *Phys. Status Solidi (RRL) Rapid Res. Lett.* 10 (6) (2016) 443–447.
- [20] N.E. Grant, V.P. Markevich, J. Mullins, A.R. Peaker, F. Rougier, D. Macdonald, J.D. Murphy, Permanent annihilation of thermally activated defects which limit the lifetime of float-zone silicon, *Phys. Status Solidi (A)* 213 (11) (2016) 2844–2849.
- [21] L.E. Black, W.M.M.E. Kessels, $\text{PO}_x/\text{Al}_2\text{O}_3$ stacks: Highly effective surface passivation of crystalline silicon with a large positive fixed charge, *Appl. Phys. Lett.* 112 (20) (2018) 201603.
- [22] J. Melskens, R.J. Theeuwes, L.E. Black, W.-J.H. Berghuis, B. Macco, P.C.P. Bronsveld, W.M.M. Kessels, Excellent passivation of n-type silicon surfaces enabled by pulsed-flow plasma-enhanced chemical vapor deposition of phosphorus oxide capped by aluminum oxide, *Phys. Status Solidi (RRL) Rapid Res. Lett.* 15 (1) (2021) 2000399.
- [23] L.E. Black, M. Ernst, R. Theeuwes, J. Melskens, D. Macdonald, W.M.M.E. Kessels, Self-aligned local contact opening and n+ diffusion by single-step laser doping from $\text{PO}_x/\text{Al}_2\text{O}_3$ passivation stacks, *Sol. Energy Mater. Sol. Cells* 217 (2020) 110717.
- [24] Y. Zhu, Z. Hameiri, Review of injection dependent charge carrier lifetime spectroscopy, *Prog. Energy* 3 (1) (2021) 012001.
- [25] L.E. Black, D.H. Macdonald, Accounting for the dependence of coil sensitivity on sample thickness and lift-off in inductively coupled photoconductance measurements, *IEEE J. Photovoltaics* 9 (6) (2019) 1563–1574.
- [26] D.B.M. Klaassen, A unified mobility model for device simulation—I. Model equations and concentration dependence, *Solid-State Electron.* 35 (7) (1992) 953–959.
- [27] D.B.M. Klaassen, A unified mobility model for device simulation—II. Temperature dependence of carrier mobility and lifetime, *Solid-State Electron.* 35 (7) (1992) 961–967.
- [28] A. Schenk, Finite-temperature full random-phase approximation model of band gap narrowing for silicon device simulation, *J. Appl. Phys.* 84 (7) (1998) 3684–3695.
- [29] P.P. Altermatt, A. Schenk, F. Geelhaar, G. Heiser, Reassessment of the intrinsic carrier density in crystalline silicon in view of band-gap narrowing, *J. Appl. Phys.* 93 (3) (2003) 1598–1604.
- [30] K. Bushick, E. Kioupakis, Phonon-assisted Auger-Meitner recombination in silicon from first principles, *Phys. Rev. Lett.* 131 (2023-08) 076902.
- [31] P.P. Altermatt, F. Geelhaar, T. Trupke, X. Dai, A. Neisser, E. Daub, Injection dependence of spontaneous radiative recombination in crystalline silicon: Experimental verification and theoretical analysis, *Appl. Phys. Lett.* 88 (26) (2006) 261901.
- [32] L. Huldt, Band-to-band Auger recombination in indirect gap semiconductors, *Phys. Status Solidi (A)* 8 (1) (1971) 173–187.
- [33] D. Hill, P.T. Landsberg, H. Fröhlich, A formalism for the indirect Auger effect. I, *Proc. R. Soc. A* 347 (1651) (1976) 547–564.
- [34] W. Lochmann, Phonon-assisted Auger recombination in indirect gap semiconductors, *Phys. Status Solidi (A)* 45 (2) (1978) 423–432.
- [35] W. Lochmann, A. Haug, Phonon-assisted Auger recombination in Si with direct calculation of the overlap integrals, *Solid State Commun.* 35 (7) (1980) 553–556.
- [36] A. Haug, W. Schmid, Recombination mechanism in heavily doped silicon, *Solid-State Electron.* 25 (7) (1982) 665–667.
- [37] D.B. Laks, G.F. Neumark, A. Hangleiter, S.T. Pantelides, Theory of interband Auger recombination in n-type silicon, *Phys. Rev. Lett.* 61 (1988) 1229–1232.
- [38] D.B. Laks, G.F. Neumark, S.T. Pantelides, Accurate interband-Auger-recombination rates in silicon, *Phys. Rev. B* 42 (1990) 5176–5185.
- [39] M. Govoni, I. Marri, S. Ossicini, Auger recombination in Si and GaAs semiconductors: Ab initio results, *Phys. Rev. B* 84 (2011) 075215.
- [40] P.P. Altermatt, F. Geelhaar, T. Trupke, X. Dai, A. Neisser, E. Daub, Injection dependence of spontaneous radiative recombination in c-Si: experiment, theoretical analysis, and simulation, in: NUSOD '05. Proceedings of the 5th International Conference on Numerical Simulation of Optoelectronic Devices, 2005., 2005, pp. 47–48.
- [41] A. Hangleiter, R. Häcker, Enhancement of band-to-band Auger recombination by electron-hole correlations, *Phys. Rev. Lett.* 65 (1990) 215–218.
- [42] A. Fell, T. Niewelt, B. Steinhauser, F.D. Heinz, M.C. Schubert, S.W. Glunz, Radiative recombination in silicon photovoltaics: Modeling the influence of charge carrier densities and photon recycling, *Sol. Energy Mater. Sol. Cells* 230 (2021) 111198.
- [43] J.M. Dorkel, P. Leturcq, Carrier mobilities in silicon semi-empirically related to temperature, doping and injection level, *Solid-State Electron.* 24 (9) (1981) 821–825.
- [44] M. Takeshima, Enhancement of Auger recombination in semiconductors by electron-hole plasma interactions, *Phys. Rev. B* 28 (1983) 2039–2048.
- [45] P. Zheng, F.E. Rougier, D. Macdonald, A. Cuevas, Measurement and parameterization of carrier mobility sum in silicon as a function of doping, temperature and injection level, *IEEE J. Photovoltaics* 4 (2) (2014) 560–565.
- [46] P. Zheng, F.E. Rougier, D. Macdonald, A. Cuevas, Parameterization of carrier mobility sum in silicon as a function of doping, temperature and injection level: Extension to p-type silicon, in: Proc. 40th IEEE Photovoltaic Specialist Conf., 2014, pp. 0129–0134.
- [47] F. Schindler, M. Forster, J. Broisch, J. Schön, J. Giesecke, S. Rein, W. Warta, M.C. Schubert, Towards a unified low-field model for carrier mobilities in crystalline silicon, *Sol. Energy Mater. Sol. Cells* 131 (2014) 92–99.
- [48] J. del Alamo, S. Swirhun, R.M. Swanson, Simultaneous measurement of hole lifetime, hole mobility and bandgap narrowing in heavily doped n-type silicon, in: 1985 International Electron Devices Meeting, 1985, pp. 290–293.
- [49] S.E. Swirhun, Characterization of majority and minority carrier transport in heavily doped silicon (Ph.D. thesis), Stanford University, 1987.
- [50] Z. Li, A. Liu, R. Basnet, L.E. Black, D. Macdonald, H.T. Nguyen, Applications of time-resolved photoluminescence for characterizing silicon photovoltaic materials, *Semicond. Sci. Technol.* 40 (4) (2025) 045015.
- [51] P.P. Altermatt, A. Schenk, G. Heiser, A simulation model for the density of states and for incomplete ionization in crystalline silicon. I. Establishing the model in Si:P, *J. Appl. Phys.* 100 (11) (2006) 113714.
- [52] P.P. Altermatt, A. Schenk, B. Schmidthüsen, G. Heiser, A simulation model for the density of states and for incomplete ionization in crystalline silicon. II. Investigation of Si:As and Si:B and usage in device simulation, *J. Appl. Phys.* 100 (11) (2006) 113715.
- [53] D.C. Meeker, Finite element method magnetics, version 4.2 (28feb2018 build), 2018, URL <http://www.femm.info>.
- [54] A.B. Sproul, Dimensionless solution of the equation describing the effect of surface recombination on carrier decay in semiconductors, *J. Appl. Phys.* 76 (5) (1994) 2851–2854.